remote sensing

MDPI

Article

Insights into Deformation and Mechanism of a Reactivated Landslide Occurrence from Multi-Source Data: A Case Study in Li County, China

Yingjin Du [1], Kun He [1,*], Xiewen Hu [1] and Hongsheng Ma [2]

[1] Faculty of Geosciences and Engineering, Southwest Jiaotong University, Chengdu 610031, China; dyj@swjtu.edu.cn (Y.D.); huxiewen@swjtu.edu.cn (X.H.)
[2] Sichuan Highway Planning, Survey, Design and Research Institute Ltd., Chengdu 610041, China
* Correspondence: hekun@swjtu.edu.cn

Abstract: The investigation of reactivated landslides in the alpine-canyon areas suffers the difficult accessibility of precipitous terrain. In particular, when reactivated landslides occur along the major roads, efforts are focused on measuring ground surface displacements during road construction. Nevertheless, the ancient landslide deposits may reactivate after several years of road operation, while they show a stable state during the road construction. The characterization of this type of reactivated landslides is challenging, due to their complex mechanism and the limited monitoring data. Appropriate multi-source data can provide insights into deformation fields and enhance the understanding of landslide mechanisms, ensuring the outperformance of remedial works. This paper reports a recent Tangjiawan reactivated landslide along the Wenchuan-Maerkang Highway in Li County, China. The outcomes, including satellite InSAR, in situ real-time monitoring, and detailed ground and UAV investigation, conducted at this landslide are presented. Early deformation of the reactivated landslide began from 2019, with an InSAR-derived velocity of −11.7 mm/year, furthermore, a significant subsidence of about 21.2 mm, which occurred within a span of only 12 days from 3 June 2020 to 15 June 2020, was observed. The deformation characteristics derived from in situ monitoring during the remedial works were likely firstly associated with the initial unreinforced slope condition and the heavy rainfall. Subsequently, the displacement evolution transformed into deformation induced by time-dependent reduction in slope strength under rainfall conditions. The existing of unconsolidated deposits derived from ancient landslides, along with a fragile geo-structure consisting of rock blocks and gravels interlayered with breccias, exacerbated by large relief created a predisposition for landslide reactivation. Furthermore, 13 days of antecedent cumulative rainfall totaling 224.5 mm directly triggered the occurrence of a landslide event. The significance and implications of integrating multiple monitoring techniques are emphasized.

Keywords: reactivated landslide; deformation; mechanism; integrated monitoring

check for updates

Citation: Du, Y.; He, K.; Hu, X.; Ma, H. Insights into Deformation and Mechanism of a Reactivated Landslide Occurrence from Multi-Source Data: A Case Study in Li County, China. *Remote Sens.* **2024**, *16*, 1317. https://doi.org/10.3390/rs16081317

Academic Editor: Sandro Moretti

Received: 20 February 2024
Revised: 2 April 2024
Accepted: 5 April 2024
Published: 9 April 2024

Copyright: © 2024 by the authors. Licensee MDPI, Basel, Switzerland. This article is an open access article distributed under the terms and conditions of the Creative Commons Attribution (CC BY) license (https://creativecommons.org/licenses/by/4.0/).

1. Introduction

Landslides are a significant concern in the field of geomorphology for road planning, design, construction, and maintenance [1–5]. Particularly in the areas characterized by alpine-canyon terrain, active tectonism, intense seismic activities, and weak rock mass, landslides not only occur in the form of new landslide, but they also exhibit as the reactivation of ancient landslide deposits [6–8].

The construction of major roads and highways on mountain slopes necessitates attention to anthropogenic activities such as slope excavating, which can significantly increase the likelihood of reactivated landslide occurrences [9–11]. However, little emphasis has been placed on monitoring slope activity for landslides that do not reactivate due to excavation but fail sometime after the completion of construction. Once a reactivated landslide is detected along the road, it is important to investigate its deformation characteristics,

reveal the prerequisite and triggering factors, and indicate whether this landslide could reactivate catastrophically and induce devastating aftermath [12–14]. Enhanced efforts have been made to understand the characteristics and mechanisms of reactivated landslides, the deformations of which are mainly induced by precipitation, water level fluctuation and anthropogenic activity [15–17]. For instance, Li et al. [18] reported the 2019 Leidashi reactivated landslide with a volume of 2.2×10^6 m^3 triggered by short-term but continuous heavy rain, which damaged two main roads and 44 anti-sliding piles. Zhang et al. [19] investigated the 2019 Yahuokou landslide reactivation induced by rainfall, with a volume of 3.92×10^6 m^3 debris that slid from the slope, and causing road disruption at the slope toe. Notti et al. [20] studied a rotational landslide in November 2016 in the upper Tanarello stream basin (NW Italy) reactivated by an extreme rainfall event, resulting in the complete collapse of two buildings and a section of the main road. In some of these cases, many attempts focus on the landslide reactivated mechanisms using pre-event rainfall data and post-event geomorphologic features [6,20,21]. Post-event deformation evolutions, in particular, of partially reactivated landslides which are subjected to remedial works in order to explore the deformation behaviors during the construction period, are often not considered. Consequently, the reconstruction of landslide evolution cannot be solely based on in situ measurement data acquired during the events. Instead, a comprehensive strategy that incorporates the entire duration of pre-event and post-event monitoring, as well as field survey data, should be adopted.

Relevant to the absence of in situ monitoring data, remote sensing techniques present significant advantages for landslide analysis [22–24]. Particularly, they are an excellent tool to reveal landslide deformation during the pre-event phase. For decades, among various remote sensing techniques, increasing contributions have been provided by Interferometric Synthetic Aperture Radar (InSAR), which exploits the phase difference between two SAR images acquired at different times over the same area, offering measurements of ground surface displacement and velocity along the radar line of sight (LOS) direction; it is currently one of the foremost methods for landslide deformation monitoring [25–28]. Numerous successful cases evidence the noteworthy preponderances of satellite InSAR in monitoring daily deformation [29,30], examining precursory movements [31,32], detecting wide-region slope deformations [33,34], and assisting the analysis of landslide mechanisms [35].

For the post-reactivation phase, especially when remedial works are performed, it is of utmost importance to center on the continuous monitoring of the slope deformations [36–39]. In situ real-time monitoring strategies are often employed to analyze landslide behaviors and to follow the remedial work performance, during and after its implementation [40–42]. The prime objective of in situ real-time monitoring is to evaluate the efficacy of the intervention by means of ground surface, crack, deep displacement and associated triggering factors analysis, which can provide essential information on the dynamics and evolution of the landslide during and after remedial works. The integration of data from various sources can effectively tackle these challenges and uncover properties of the phenomenon that would otherwise remain unknown.

This paper aims to analyze the Tangjiawan reactivated landslide by means of a combined analysis of InSAR-based and in situ real-time monitoring data, which were acquired using an integrated remote sensing monitoring system for this case. Coupled with geological and geomorphological observations from detailed and immediate field investigations, the integration of the monitoring datasets has yielded a comprehensive perspective on the deformation field of the landslide before reactivation, during and following remedial works, and enabled the unravelling of key features concerning its mechanisms and behavior. This study emphasizes the benefits and implications of integrating monitoring data from diverse sources to enhance the comprehension of reactivated landslides along major road infrastructure. This approach offers a more comprehensive understanding of the dynamics and behavior of reactivated landslides, thereby contributing to improved road engineering practices.

2. Study Area

2.1. Geological Background

The ancient landslide falls in a complex shear tectonic system, involving the "S"-shaped tectonic structure of Xuecheng and the northwest-strike structure of Maerkang, dominated by fold structures of reverse anticlinorium and synclinorium (Figure 1c). A great deal of "S"-shape-like folds and faults are observed in the study area, attributed to the "S"-shaped tectonic structure of Xuecheng, with strikes of 60° and 220° in the northeast and southwest direction, respectively. The bedrock in the landslide zone belongs to dark gray phyllite, interlayered with thin-bedded quartz sandstone, with cleavage with an occurrence of 265°∠70°~85°, corresponding to the lower Weiguan formation of the Devonian period of the Paleozoic era. Two sets of discontinuities are observed with occurrences of 345°∠45° and 200°∠65°, respectively, which result in the rock masses presenting a fractured structure. The main loose deposits of the study area are collapsed deposits, landslide deposits and alluvium deposits of the Quaternary Holocene. The study area was characterized by active tectonic movements, with frequent earthquakes caused by the collision between the Indian Ocean Plate and the Eurasian Plate, including the 2008 Wenchuan earthquake (Ms 8.0), 66 km away from the study site. Severe earthquakes could influence the stability of steep slopes within the area and cause geological disasters. Nevertheless, only two small earthquakes with a magnitude of less than 3.0 were captured 35 km away from the landslide site (https://news.ceic.ac.cn/, accessed on 20 March 2024.).

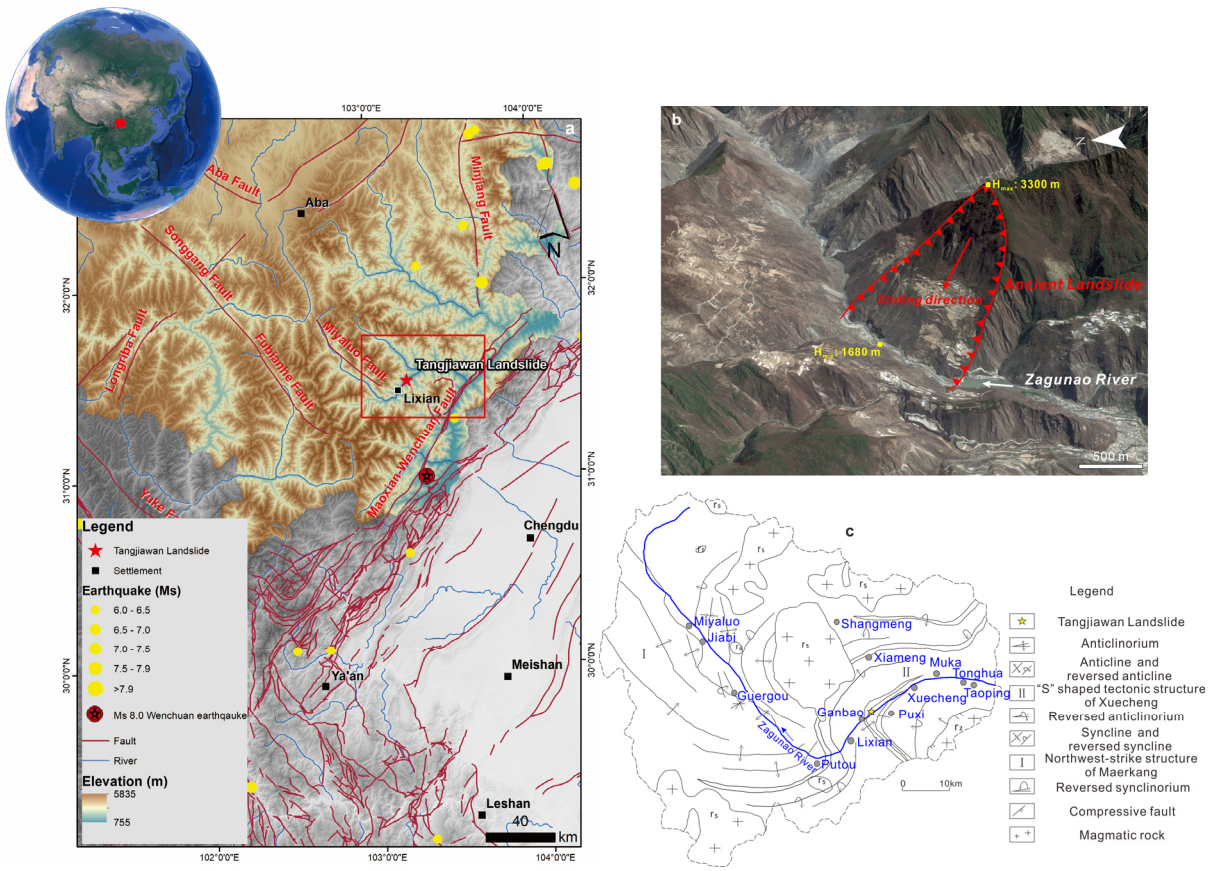

Figure 1. (**a**) Regional geological map of the study area. (**b**) Plan view of the ancient landslide. (**c**) Tectonic map of the study area.

2.2. Geomorphology

The study area is situated on the southeastern margin of the Tibet Plateau, characterized by its lofty elevation and rugged terrain. The landscape is defined by deep canyons surrounded by high mountains (Figure 1a). The elevation range of the ancient landslide

area spans from 1600 m to 3300 m, with the peak of the slope positioned at an approximate elevation of 3300 m and the toe situated in the ravine bed of the Zagunao River at around 1680 m, resulting in a vertical variance of approximately 1620 m (Figure 1b).

2.3. Climate and Hydrogeology

The research area is located within a subtropical plateau monsoon climate zone. The average annual precipitation from 2005 to 2022 ranged between 650 and 1000 mm, with a peak daily rainfall of 55.9 mm. The wet season spans from May to September, during which time 80% of the yearly precipitation occurs, often manifesting as rainstorms or heavy downpours. A rain gauge positioned on the pre-existing anti-slide piles recorded a cumulative rainfall of 224.5 mm from 10 May to 22 June, in the year 2022 (Figure 2). The groundwater in the study area is predominantly stored within unconsolidated soil pores and fractured rock fissures.

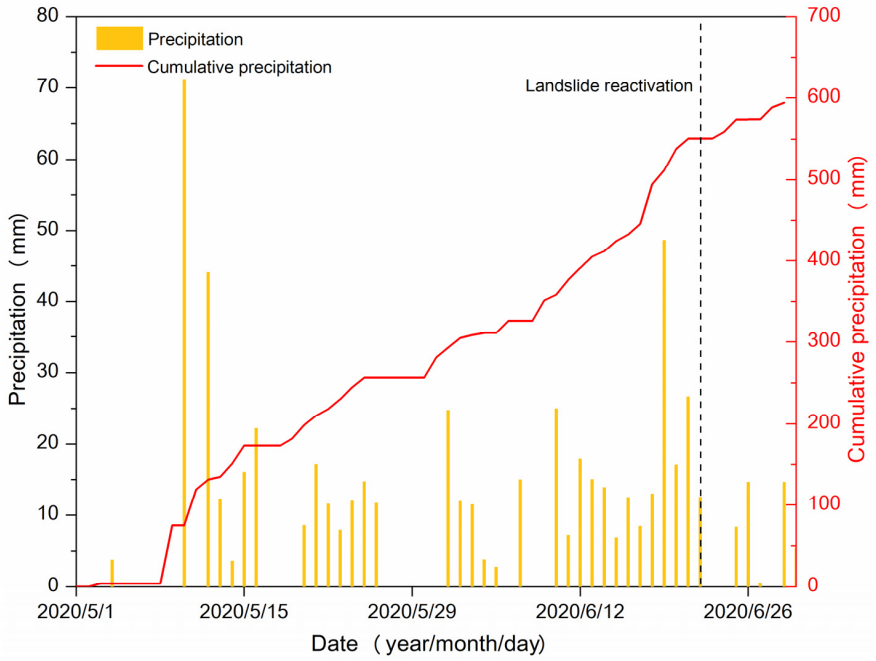

Figure 2. Daily and cumulative precipitation of May to June 2020 in the study area (Dash line means the occurrence of the landslide reactivation).

2.4. General Description of the Ancient Landslide and Recent Reactivation

The Tangjiawan reactivated landslide occurred in a slope with a historical event of ancient landslide occurrence, presenting a chair-like shape in its planform morphology, with a length along the sliding direction of 2120 m, an average lateral width of 1600 m, with a total area of approximately 2.96 km^2, and a total volume of about 1.18×10^8 m^3 (Figure 1b). The local collapse of the Tangjiawan landslide began from 22 June 2020; however, the deformation signs including road subsidence and cracks were observed since June 2019. The remedial work of concrete grouting was carried out in 2019 but failed in stabilizing the slope.

3. Methodology

After the severe deformation and failure of the slope, emergency and permanent remedial works were performed, through a construction period of November 2020 to July 2022 (Figure 3), with the construction work conducted by Sichuan Highway Planning, Survey, Design and Research Institute Ltd. The InSAR technique was deployed to reveal the pre-reactivation landslide evolution; then, ground and UAV investigations were carried out to identify the landslide characteristics, and the in situ real-time monitoring system was conducted to achieve the outperformance of the remedial works (Figure 4).

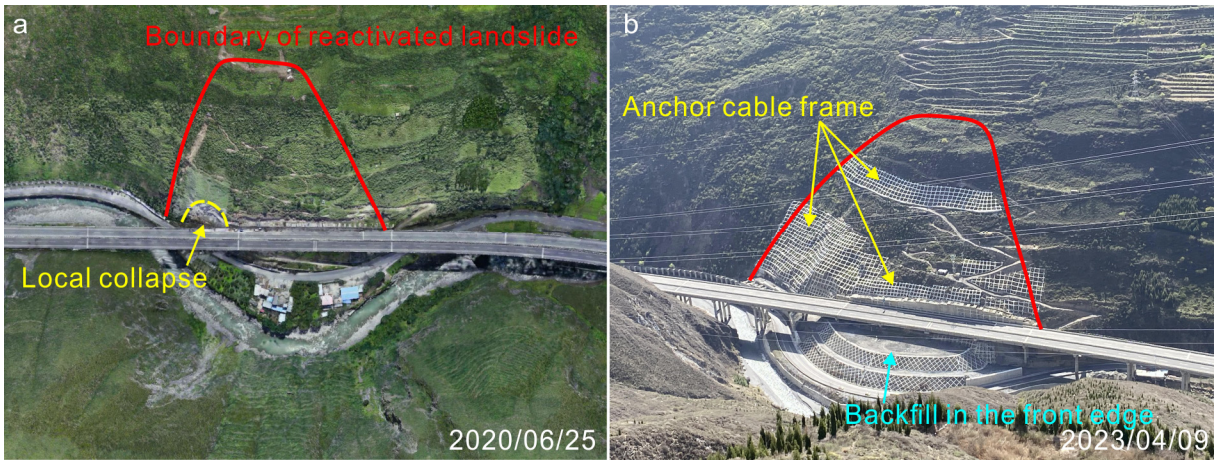

Figure 3. Geomorphologic characteristics of (**a**) pre-remediation and (**b**) post-remediation.

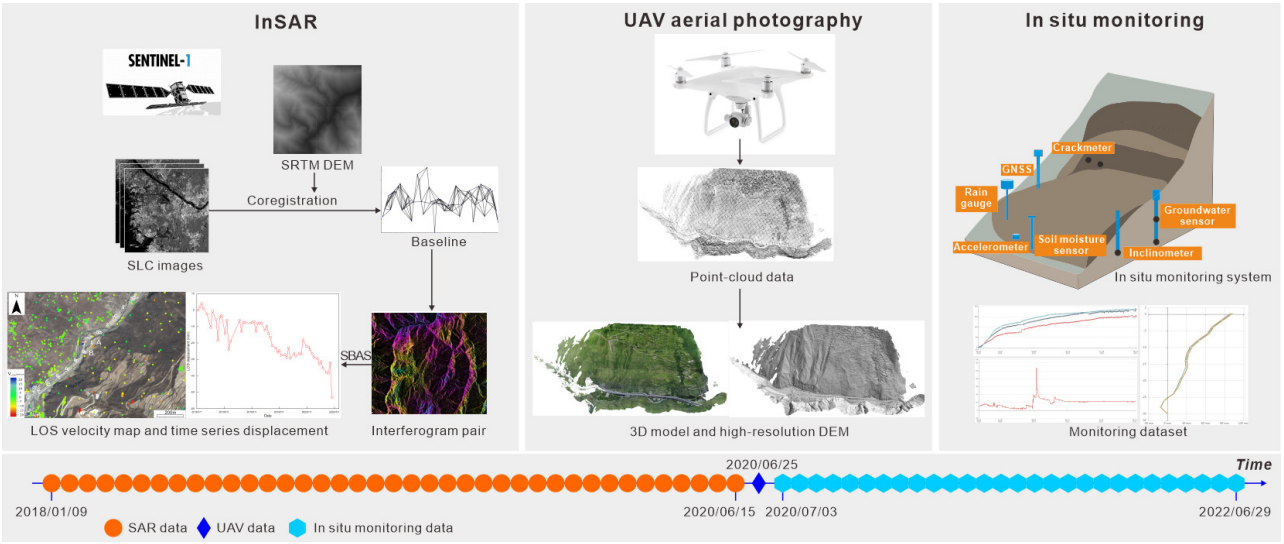

Figure 4. Integrated monitoring dataset and temporal coverage from different sources.

3.1. Ground and UAV Investigations

The detailed field investigations focusing on the Tangjiawan landslide were conducted from 22 June 2020 to 31 December 2020. Firstly, the location and occurrence of all the cracks, the deformation signs of infrastructures, and the boundaries of the reactivated landslide were identified. Six boreholes were drilled and cored to explore the geo-structures of the landslide. In total, 1568 orthoimages were acquired using an unmanned aerial vehicle, DJI Phantom 4 Pro (SZ DJI Technology Co Ltd, Shenzhen, China), and then a stereo aerial map and an orthophoto map were created using ContextCapture software (version 10.20).

3.2. InSAR Technique

Sentinel-1 Single Look Complex (SLC) products in Interferometric Wide (IW) mode were collected to derive the surface deformation in the study area. The Sentinel-1 satellite performs C-band SAR imaging and provides long-term monitoring with a revisit cycle of a minimum of 6 days. The delivered images have 5 (in range) × 20 (in azimuth) m spatial resolution. As indicated from the optical images, the main direction of the slope is toward the northwest, which causes a foreshortening effect in ascending data. Therefore, 72 Sentinel-1 images (Track 62) in descending orbital direction spanning from 9 January 2018 to 15 June 2020 were collected to generate a stack of 237 interferograms (Figure 5). The stacks of SAR images were processed using ISCE [43]. The 30 m Shuttle Radar Topography

Mission (SRTM) digital elevation model was used to remove topographic phases and geocode interferograms, and the Generic Atmospheric Correction Online Service (GACOS) was used to remove the atmospheric phase [44], and displacement and time series were derived using the StaMPS package [45].

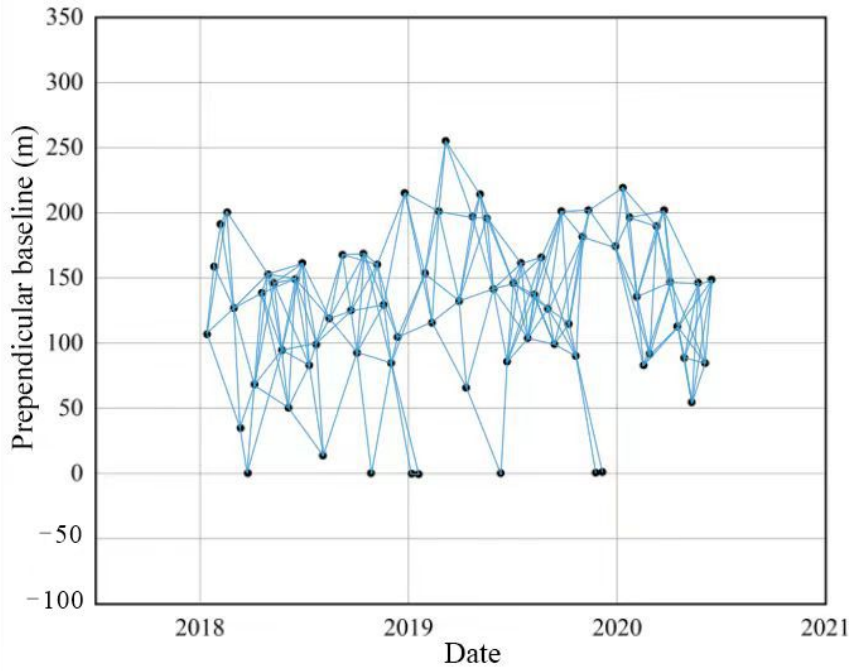

Figure 5. Temporal and perpendicular baselines of the InSAR processing.

3.3. In Situ Real-Time Monitoring

A monitor network of 12 permanent Differential Global Navigation Satellite System (GNSS) stations, 4 crack meters, 3 soil moisture sensors, 4 inclinometers, 3 groundwater monitoring stations and 2 accelerometers was deployed on the landslide in the aftermath of the June 2020 reactivation (Figure 6). The GNSS stations were set on the slope surface to obtain the ground surface displacement, and the displacements in the landslide area during the monitoring period were analyzed through the cumulative displacement and deformation velocity changes of each monitoring point. The cracks (including cracks on the infrastructures) were monitored by implementing crack meters to unravel the development tendency of cracks. The utilization of inclinometers was imperative to ascertaining the depth of the sliding surface and in monitoring the magnitude, velocity, and direction of landslide displacement. The soil moisture meters were set up to monitor the soil moisture content on the slope surface, and the groundwater monitoring gauges were installed to obtain the groundwater level of the study area. The accelerometers were installed on the anti-slide piles to measure the tilt of the structures. Moreover, near the boundary of the landslide, a rain gauge for monitoring precipitation was installed in an unobstructed and stable area. The deadline for all data statistics presented in this study is 29 June 2022.

3.4. Geotechnical Test

The physical mechanic properties of sliding zone soils are vital for unveiling the mechanism of landslides. In order to determine the properties of the soils, geotechnical tests were performed in a laboratory, including index properties, such as specific gravity, density, and Atterberg limits. In addition, a direct shear test was conducted to obtain the shear strength of the soils within the sliding zone. Ten samples were collected from drilling holes ZK01 and ZK02 in the front and middle parts of the study area.

Figure 6. In situ real-time monitoring network and the locations of different instruments.

4. Characteristics of the Reactivated Landslide

Based on the field investigation, borehole drilling and UAV photogrammetry, reactivated area and depth were identified. The reactivated landslide shows a chair shape in the plane, spanning a length along the sliding direction of 100 m and reaching a maximum width of 100 m. The landslide covers an area of about 10×10^3 m^2, with a summit altitude of the area of approximately 1855 m a.s.l and a minimum altitude near the foot of approximately 1685 m a.s.l. The toe of reactivated area falls into the K93 + 900~K94 + 200 section of the Wenchuan-Maerkang Highway. The gradient of front edge is about 20~30°, while the middle and rear parts have a slope gradient of 30~40°, and the main sliding direction is 300° (Figure 7). The determination of the thickness of the sliding mass is achieved through the process of borehole drilling, which is about 25.3~40.1 m, with an average thickness of 35.0 m; thus, the reactivated landslide has a volume of about 350×10^3 m^3 (Figure 8).

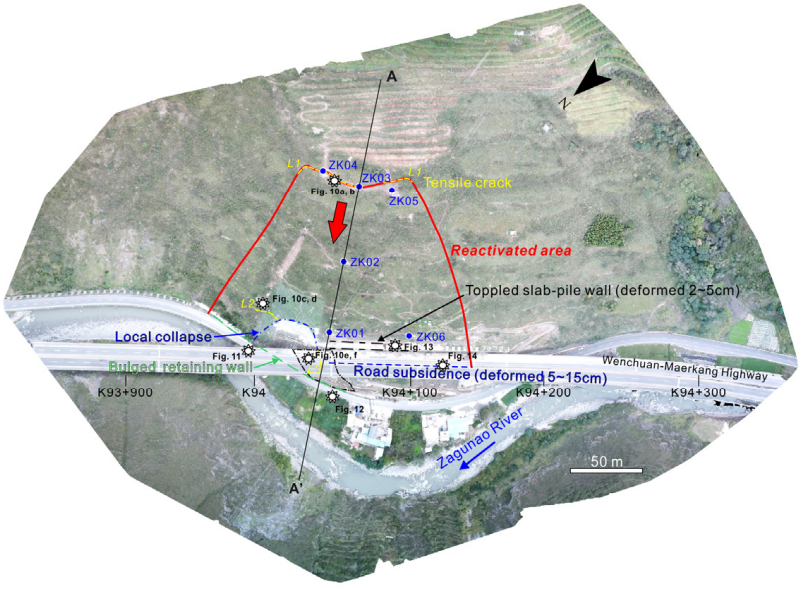

Figure 7. The geomorphological map of the reactivated landslide and the distribution of in situ investigation points. The base map is a UAV orthophoto from 25 June 2020.

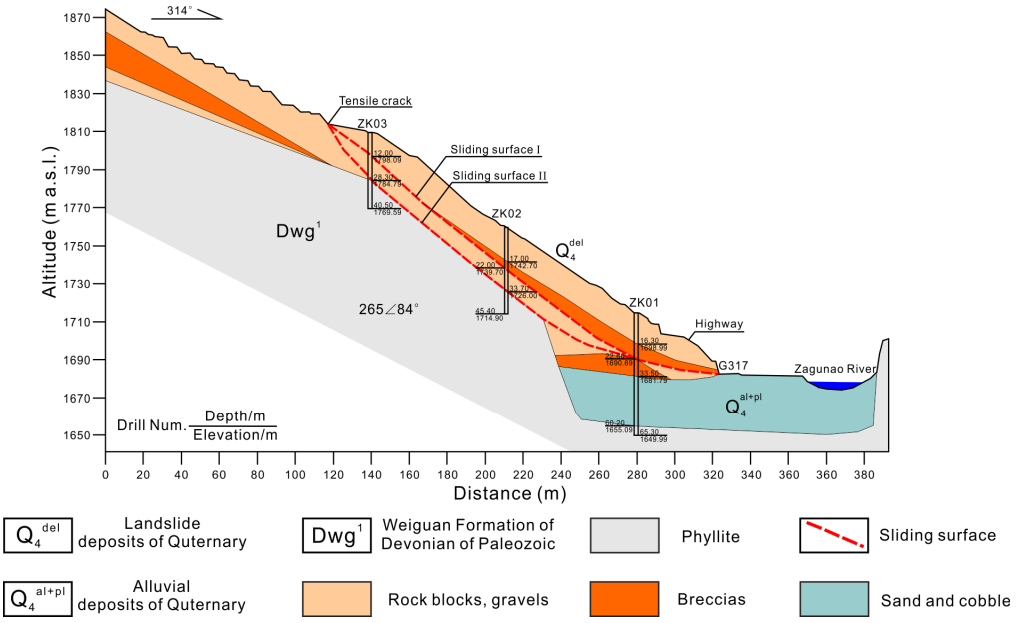

Figure 8. Longitudinal profile of the reactivated landslide (section A–A' in Figure 7).

4.1. Structural and Material Characteristics

Based on the findings from borehole drilling, exploratory trench testing, and field outcrop investigations, it has been determined that the sliding mass primarily consists of rock blocks, gravels, and breccias (Figure 9). The rock blocks and gravels are characterized by loose structuring with a medium density and a grayish-brown color, and good permeability but a limited water retention capacity. Similarly, the breccias also present a loose structure, mainly medium density, with a gray-brown color, good permeability and water retention ability. The soil composition within the sliding masses is heterogeneous; while rock blocks and gravels have high porosity and strong permeability characteristics, breccias exhibit low porosity and poor permeability properties. Drillings indicate that the clay particles are concentrated in the breccias locally, where the smooth mirrors are also observed with a dip angle of 10~25° (Figure 9c,d).

Multiple slip zones were observed within the reactivated landslide, which is generally steep in the upper and middle parts and gentle in the lower part longitudinally. The middle part of the landslide mainly deforms and slides along the soil–rock interface, with a dip angle of about 36°, while the front edge primarily passes through the gravel and breccia layers, with an inclination of about 5° (Figure 8). The material in the slip zone predominantly contains grayish-brown breccias evolved from phyllite, containing clay, with a particle size of 20~200 mm for about 10% and 2~20 mm for about 50%. The sliding bed is phyllite, belonging to the Devonian Weiguan formation, preponderantly including fractured phyllite. Owing to the regional tectonic influence, the rock mass exhibits a relatively fractured state, characterized by the development of numerous joints and fissures.

4.2. Ground Deformation

A detailed field investigation revealed that the deformation and reactivation signs began on 22 June 2020, which included tensile cracks in the ground surface and a local collapse at the front edge of the slope.

Figure 9. Borehole drillings reveal the structure of the landslide. (**a**) Angular revealed by ZK04. (**b**) Rock blocks and debris from ZK03. (**c**,**d**) Breccia soil from ZK01 and ZK02, respectively.

The ground surface tensile cracks involved three major cracks, mostly located along the boundary of the landslide (rose diagram of the crack strike in Figure 10). The crack L1 had developed at the rear edge, comprising several small cracks, with a length of approximately 100 m, a width of about 1~10 cm and a maximum drop of 180 cm. The strike of L1 was 210~230°, and was nearly parallel to the road direction (Figure 10a,b). The crack L2 was located at the right part of the landslide, belonging to the extension of the rear boundary of the local collapse, with a length of about 30 m, a width of about 1~10 cm, a drop of approximately 20~100 cm, and a strike of 210~230° (Figure 10c,d). The crack L3 was near the front edge of the local collapse, mainly composed of cracks parallel and oblique to the road. The width of the crack was about 0.2~2 cm, the length was about 5~20 m, and the strikes were 210~230° and 350°, respectively Figure 10e,f).

The local collapse had occurred on 22 June 2020, which was located in the right-lower part of the reactivated landslide (Figure 7). This local collapse had a length along the sliding direction of 30 m, and a width of 20 m, covering an area of 600 m^2. Based on the geometry measurement of the surrounding slope, the collapse had a thickness of about 2 m, corresponding to a shallow landslide (Figure 11). The volume of this area was approximately 1200 m^3. The slide direction of this local collapse was approximately 30°, and several tensile cracks and fissures formed in its rear part.

The 210~230° orientation and progressive widening of these cracks, as well as the local collapse, are indicative of the overall shear strength reduction of the slope. The development of tensile cracks probably marked the pre- and entire failure creep deformation. Such occurrences afford a reasonable lead time, representing the temporal interval between the initial observations of precursors and the occurrence of a major failure event, with the aim of providing a timely early warning.

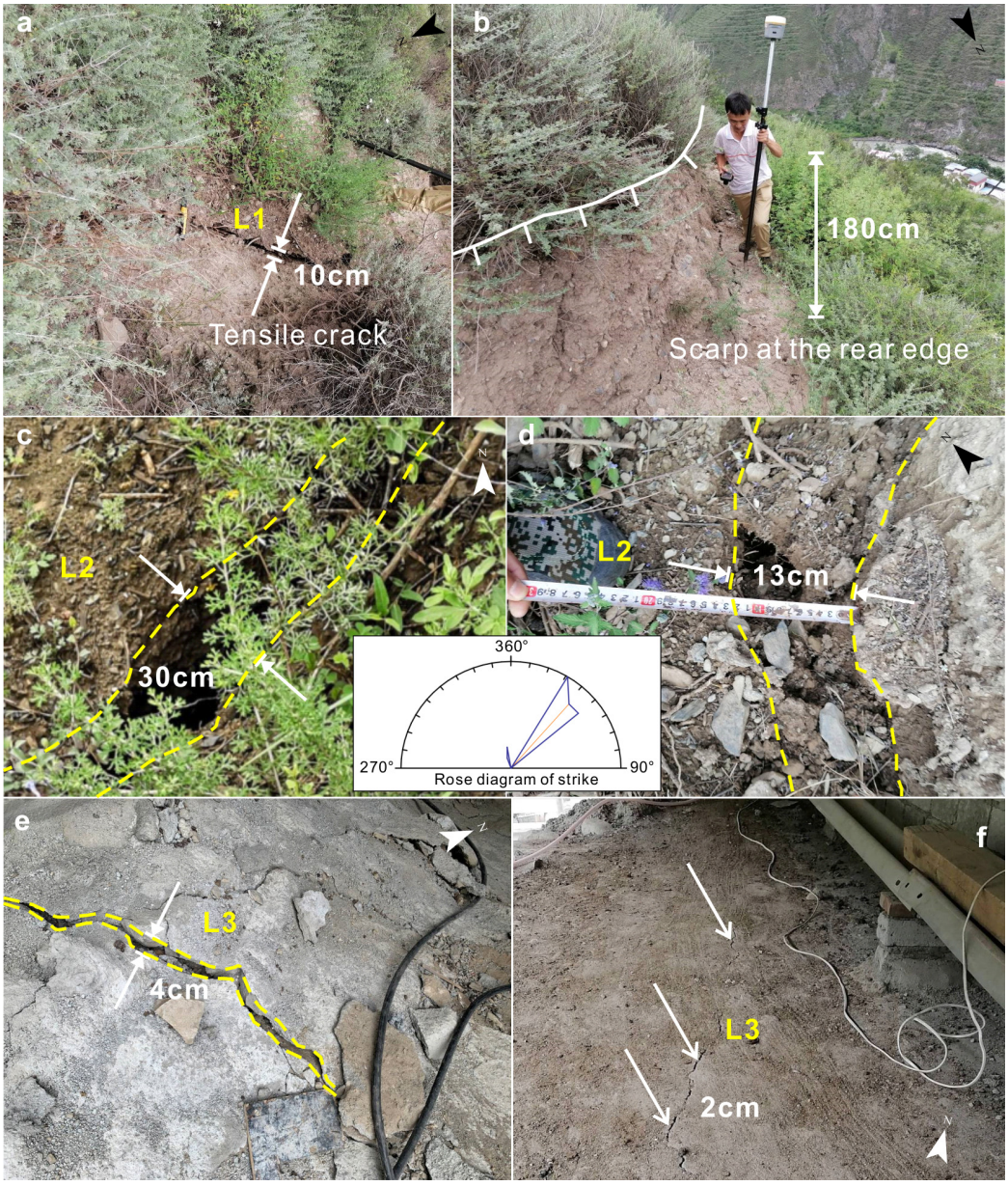

Figure 10. Cracks developed in the landslide area and their rose diagram of strike. (**a**,**b**) Tensile crack L1 at the crown of the reactivated landslide. (**c**,**d**) Tensile crack L2 observed in the vicinity of the local failure. (**e**,**f**) Tensile cracks at the ground surface at the slope toe.

4.3. Infrastructure Deformation

The deformation of infrastructure began from 2019 with slight signs of deformation on the road surface; due to the conducting of countermeasures, the deformation was not recorded. Since June 2020, the infrastructures within the landslide area were seriously damaged, which mainly included retaining walls, ditches, slab-pile walls and roads. National road G317 passes through the front edge in the form of excavation, with an excavated height of about 2~5 m, and a retaining wall with a slope ratio of about 1:0.3~1:0.5 was constructed around 2010 and has been used for nearly 10 years. On 22 June 2020, after heavy rainfall, the slope began to deform, and a bulging crack on the wall and a bulged deformation were observed (Figure 12a). Moreover, the boundary of left side of the road was a ditch with a concrete cover plate. The soil mass of this location was uplifted due to the extrusion, with a height of about 2–20 cm, and the cover plate was damaged (Figure 12b,c).

Figure 11. Local collapse occurred at the lower section of the slope. (**a**) The collapse reached the bridge. (**b**) Rock blocks distributed within the residual slope. (**c**) The failure of the slope damaged the pier of the bridge. (**d**) The rear edge of the local collapse.

Figure 12. (**a**) Bulging deformation of the retaining wall. (**b**,**c**) Uplift deformation of the cover plate of the road ditch.

A 160 m long slab-pile wall was constructed at the front edge of slope. The investigation revealed that cracks appeared on both sides of the slab-pile wall. The tensile crack appeared at the junction of the pile and lattice frame, with a width of about 5~10 cm, showing severe damage (Figure 13a). About 11 vertical cracks were observed in front of the slab-pile wall, with widths ranging from 0.1 to 0.8 cm. It was noticed that the cracks began to gradually extend from 22 June 2020 (Figure 13b). The rear edge of the slab-pile wall was a ditch constructed using concrete, where the cracks began to develop from 22 June, with a width of 1~8 cm, and progressively extended (Figure 13c,d).

Figure 13. Crack deformations of the slab-pile wall in the front edge of slope. (**a**) The crack developed in the junction of pile and lattice frame. (**b**) Crack developed on the slab-pile wall. Crack observed on different dates: (**c**) 7 July and (**d**) 5 September 2020.

A concrete retaining wall was set on the right side of the subgrade. The subsidence and tensile deformation of the retaining wall began to appear after June 2020, with the maximum subsidence reaching 12 cm; in the entire retaining wall, some sections were cracked and damaged (Figure 14).

In late June 2019, the road ground surface of the left Wen-Ma highway exhibited local subsiding, and the subsidence height reached 2~13 cm. The subgrade of this section was grouting treatment. However, since June 2020, the subgrade continued to subside (Figure 14e), and several transverse cracks appeared, with the crack width ranging from 0.2 to 2 cm (Figure 14d).

Figure 14. Deformation signs of highway and retaining wall. (**a**) Subsidence of retaining wall. (**b**) Tensile crack in the inside of road. (**c**) Crack on the retaining wall. (**d**) Crack observed on the road. (**e**) Subsidence of road after the reactivation in 2020 while the profile showing the elevation change of the road surface. (**f**) Tensile crack developed in the junction of road and retaining wall.

5. InSAR-Derived History Deformation

Figure 15 depicts the mean velocity of deformation in the LOS direction of the study area between 9 January 2018 and 15 June 2020, which is derived from the SBAS-InSAR technique. The monitored time stack has a mean LOS velocity of −18.9~6.5 mm/yr. Two monitoring points of interest are obtained near the ground surface of the Wen-Ma highway, and the mean LOS velocity of point A was about −11.7 mm/year. The subsidence area was mainly distributed along K94 + 000~K94 + 200. The landslide area suffered uneven subsidence, with a mean LOS velocity of −18~−5 mm/year.

The cumulative displacement curve of InSAR-derived monitoring points in time series can be used to identify the evolution stage of the reactivated landslide. Cumulative displacement time tendency analysis of two monitoring points in three deformation regions was conducted. Figure 16 presents the time series LOS displacement of two PS monitoring points on the front edge of the slope. The ground surface represented by point A has shown a seasonal subsidence tendency since January 2018, but a large subsidence of about 21.2 mm occurred over 12 days from 3 June 2020 to 15 June 2020. The ground surface represented by point B also has a seasonal subsidence trend during the monitoring period, with a mean LOS velocity of about −5.9 mm/year and a total displacement of 50 mm from January 2018 to June 2020. The seasonal deformation indicates that the precipitation plays an important role on the slope stability.

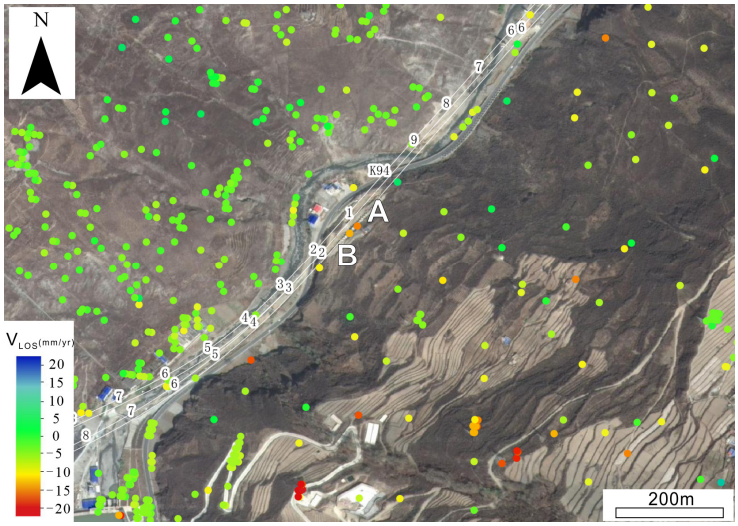

Figure 15. LOS Velocity of study area based on SBAS-InSAR (Points A and B are the selected monitoring points, while the numbers mean the mileage of the highway).

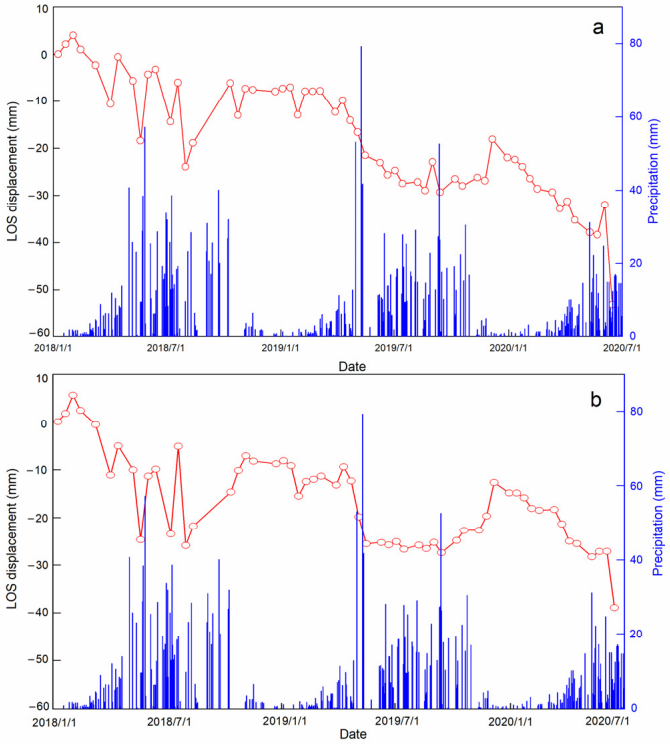

Figure 16. LOS displacement versus time of point (**a**) A and (**b**) B.

6. In Situ Real-Time Monitoring Results

6.1. The Monitoring Results of the Surface Displacement

Figure 17 depicts the monitoring results of the surface deformation of the reactivated landslide obtained from the GNSS stations. Among the 12 GNSS stations, GNSS01-03 stations are installed on the original anti-slide piles at the toe of the slope. In terms of deformation varying with time, a period of rapid deformation was recorded in the three monitoring points from 17 July to 13 November 2020, with horizontal displacement increments of 56.4 mm, 77.3 mm and 92.6 mm for GNSS01-03, respectively. Such deformation characteristics are likely attributed to the unreinforced slope condition and heavy rainfall. Subsequently, the displacement evolution transforms into that of deformation induced by time-dependent slope strength reduction under rainfall and anthropogenic activities.

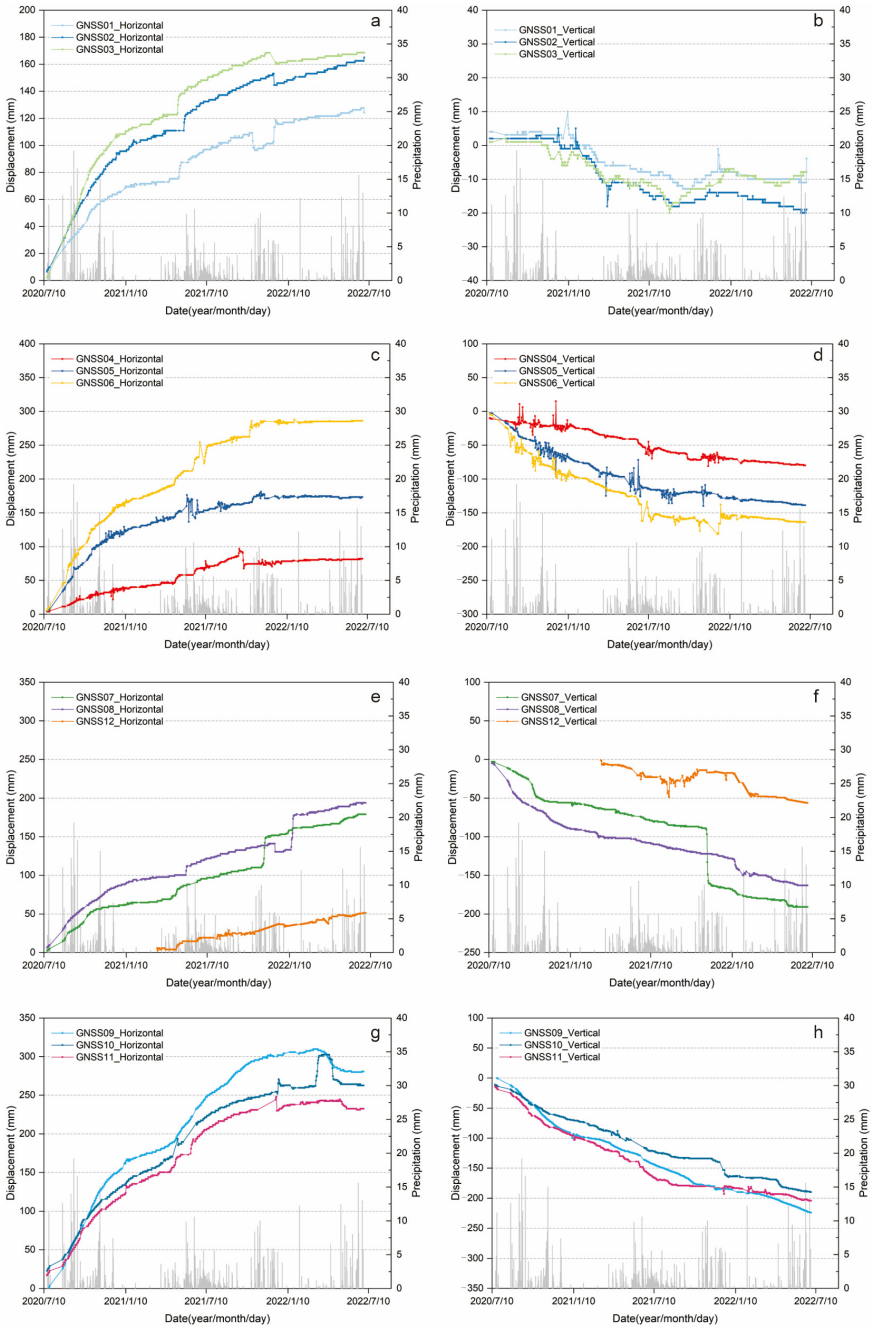

Figure 17. Displacement and precipitation versus time curves: (**a**) horizontal and (**b**) vertical displacement versus time monitored by GNSS01-03. (**c**) Horizontal and (**d**) vertical displacement versus time monitored by GNSS04-06. (**e**) Horizontal and (**f**) vertical displacement versus time monitored by GNSS07, 08 and 12. (**g**) Horizontal and (**h**) vertical displacement versus time monitored by GNSS09-11.

GNSS04-06 stations were installed on the lower part of the slope, which had a similar deformation response to GNSS01-03 after implementation until January 2021. A rapid deformation period can be observed at the onset of deformation monitoring, with horizontal displacements of 29.9 mm, 102.2 mm and 135.7 mm for GNSS04-06, respectively, but it disappeared after the countermeasures that were conducted on December 2020, and the deformation tended to be stable since December 2021.

For the ground surface of Wen-Ma Highway and the National Road G317 with GNSS07-08 and GNSS12 stations installed (GNSS12 installed on 20 March 2021), an increasing displacement over time is observed, which consists of initially rapid deformation followed by slow

increasing, due to the effective countermeasures. Notably, GNSS07 and GNSS08 present a sudden increase in both horizontal and vertical displacement in the period of 15 November 2021 to 18 January 2022, with displacement increments of 10~40 mm, indicating that the road surface deforms due to the cumulative precipitation of 95 mm in this period.

GNSS09-11 stations are installed at the right lateral boundary of the reactivated landslide, where the maximum displacement is recorded in the monitoring period, reaching 280.7 mm, 262.6 mm and 232.6 mm, respectively. Such deformation features corresponding to the countermeasures are conducted first at the sections in the vicinity of the Wenchuan-Maerkang Highway, followed by the right boundary; thus, these deformations become stable after November 2021.

6.2. The Monitoring Results of the Deep Displacement

Borehole inclinometers are the most direct way to reveal the sliding zone and to understand the subsurface deformation of the landslide. Figure 18 depicts the deep displacement data measured by four inclinometers. It can be seen the cumulative displacements of inclinometers IN-1, IN-3 and IN-4 have been increasing during the selected monitoring period, suggesting that landslide deformation is still ongoing but at a low deformation rate. Due to the IN-2 being installed on 20 April 2021, the monitoring period of 1 October to 20 October 2021 was selected, when the deep displacement was constant, showing no increasing deformation in IN-2. In addition, Figure 18 illustrates that inclinometers IN-1, IN-3 and IN-4 show obvious shear displacement at different depths, that is, the depth of the sliding zone is 10~12 m and 28~30 m in borehole IN-1, 20~22 m in borehole IN-3, and 20~22 m in borehole IN-4.

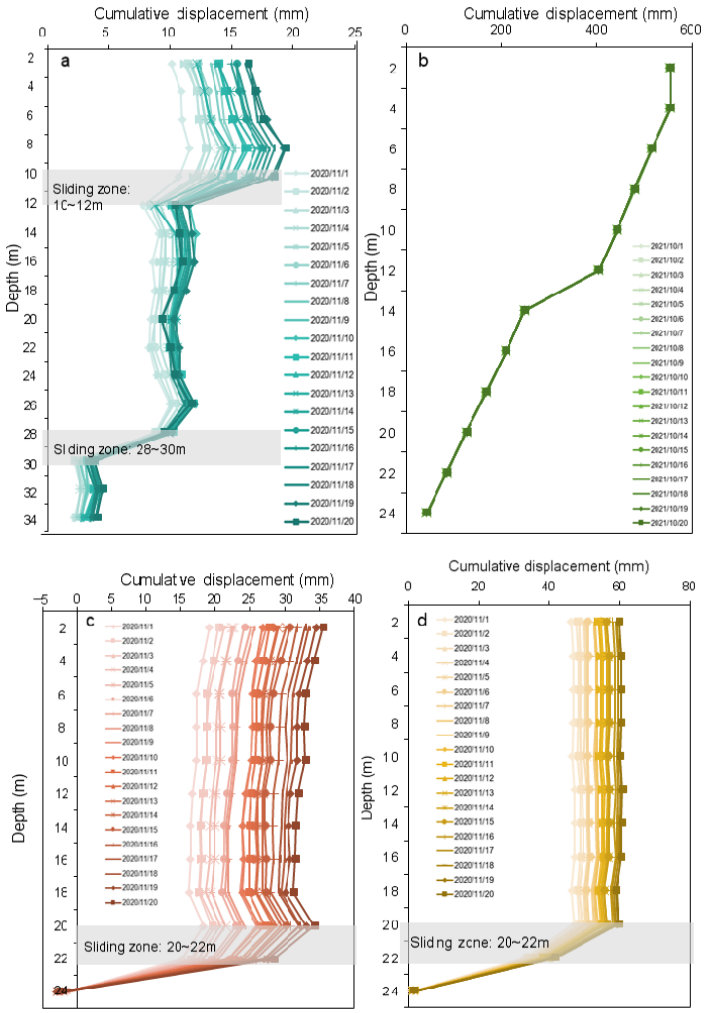

Figure 18. (**a**–**d**) Cumulative displacement of inclinometers IN01-04.

6.3. The Monitoring Results of the Crack Deformation

Crack meter 01 (CM01) and CM02 are installed on the anti-slide piles, and CM03 and CM04 are located at the rear edge of the local collapse. As shown in Figure 19, all cracks showed coherent opening rates at the early stage of the countermeasure constructing, reached displacements of 16.7 mm in crack meter 01, 51.9 mm in in CM02, 111.2 mm in CM03, and 82.9 mm in CM04, which were overprinted by short-term accelerations triggered by heavy rainfall. Hereafter, the deformation rates showed a low level, except for several intense jump points, which may be influenced by the construction of the anchor cable frame. The ground cracks (CM03 and CM04) present a tendency for high rates and greater displacements compared to the infrastructure cracks (CM01 and CM02).

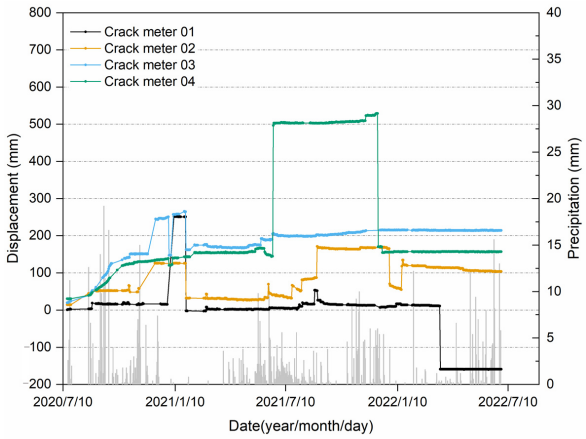

Figure 19. Displacement and precipitation versus time curves on cracks monitored by crack meters 01-04 (Grey bar is the precipitation).

6.4. The Monitoring Results of the Soil Moisture

Figure 20 depicts the change in soil moisture within the landslide area. During the monitoring period, rainy seasons were accompanied by the marked increase in the soil moisture, with soil moisture peaking in the rainy season in 2022 for SF1 and SF2 at the left boundary and middle parts of the landslide, at 19.2% and 24.8% soil moisture content, respectively, as rainfall continued to occur with heavy precipitation in this period. SF3 at the right boundary of the landslide was characterized by stable soil moisture, changing from around 5 to 10%, and the variation mode was also related to the onset of the precipitation event. The deformation of the slope was related to the increase in soil moisture. Before the main countermeasures were conducted and completed in December 2021, the increase in soil moisture induced significant deformations of the slope; nevertheless, after the remediation, the slope tended to be stable, even though soil moisture increased.

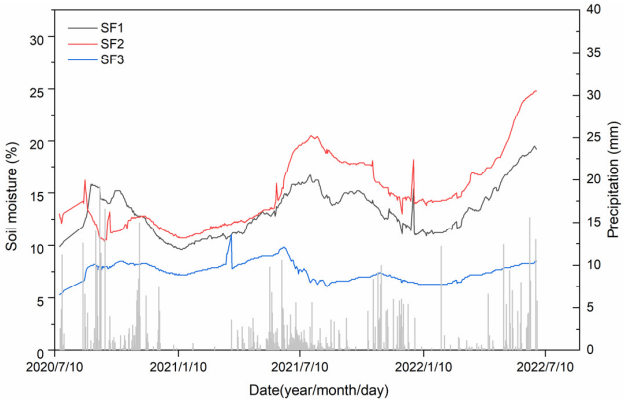

Figure 20. Soil moisture versus time curves monitored by sensors SF1-3 in Figure 6 (Grey bar is the precipitation).

7. Discussion

7.1. Factors Contributing to the Reactivated Landslide

7.1.1. Predisposing Factors

- Unconsolidated deposits derived from ancient landslide at the base of the slope

Surrounding mountainous landscape and the chair-like shape of the studied slope shows that an ancient landslide had occurred. Based on the materials indicated by the borehole drillings, the ancient landslide deposits overlie the alluvium deposits formed by the Zagunao River, indicating that a river-damming event had occurred by the ancient landslide. Moreover, the ancient accumulation layer of the landslide exhibited characteristics of high porosity, elevated water content, and a rich water medium. As previously mentioned, the sliding mass possessed a loose structure, primarily comprised of rock blocks, gravels, and breccias, with coarse particles accounting for 50~60% of its composition. The formation of a skeletal framework between the rock blocks created favorable conditions for predominant seepage. This intricate network facilitated the dominant flow of water within the landslide accumulation layer. Thus, the concentrated seepage is prone to occur then, causing the finer soil particles to be washed away, forming macropores within the rock blocks when the deposits are subjected to high-intensity precipitation, ultimately decreasing the stability of the unconsolidated landslide deposits. The residual rock blocks and gravels could be observed in the failed local collapse, which is attributed to the concentrated seepage.

- Fragile geo-structure of rock blocks and gravels interlayered with breccias

The ancient landslide deposits consist of rock blocks, gravels interlayered with breccias, in which the breccias with poor permeability are located between the rock blocks, and gravels with high permeability. A large amount of precipitation in this area is transferred to groundwater through the rock blocks and gravels and is discharged along the interlayer of breccias and bedrock. However, due to the limited drainage points, part of the groundwater is retained in the breccias layer. Under the action of the high overlying sliding mass weight pressure, the water and the breccia are strongly hydrated, that is, the breccia is argillated, and the strength of the breccia is greatly reduced and it becomes a potential slip zone.

Ten soil samples in the sliding zone were collected in the landslide area (Figure 7). Through laboratory experiments, the geotechnical properties are obtained. Table 1 lists the physical mechanics indexes of the sliding zone soils. The measured natural and saturated water content of the sliding zone soil is 7.1% and 21.3%, respectively. Regarding the peak strength to residual strength, the strength parameter of sliding zone soils decreases significantly, while cohesion decreases by 67% and the internal friction angle decreases by 33% in the natural water content condition of soils. The same shear test was conducted for the saturated condition of the samples. The cohesion decreases from 6.5 kPa to 2.0 kPa, and the internal friction angle decreases from 15.5° to 11.2° between the peak strength and residual strength. The results indicate that the strength of the sliding zone soil will be significantly weakened under the action of water infiltration. The liquid limit is 35.1%, and the plastic limit is 16.2%. The soil has a plasticity index of 18.9. When the water content reaches the plastic limit, any further increase in water content will precipitate a marked deterioration in the strength of the sliding zone soils, thereby compromising the stability of the slope. The inherent natural water content of sliding zone soils is measured at 7.1%, that is, the soils require the infiltration from rainwater to be saturated. Hence, the role of rainwater infiltration is considered as the primary factor this reactivation.

Table 1. Physical and mechanics parameters of sliding zone soils.

Natural Density (g/cm^3)	Water Content (%)		Liquid Limit (%)	Plastic Limit (%)	Plasticity Index	Peak Strength				Residual Strength			
						Cohesion (kPa)		Internal Friction Angle (°)		Cohesion (kPa)		Internal Friction Angle (°)	
	Natural	Saturated				Natural	Saturated	Natural	Saturated	Natural	Saturated	Natural	Saturated
1.94	7.1	21.3	35.1	16.2	18.9	16.5	6.5	22.6	15.5	5.5	2.0	15.1	11.2

- Large relief of the original slope

The ancient landslide has an area of 2.96 km^2, with an elevation difference of 1620 m, and an average slope of 36°, presenting a steep-gentle-steep terrain longitudinally. The rear edge of the reactivated landslide is located at the slope break zone, which belongs to the concentrated region of tension stress. The Zagunao river valley is characterized by a deep incision, showing a "V" shape, with 80 m in width near the Tangjiawan ancient landslide at the bottom of the valley and less than 20 m wide at the narrowest section. Unraveled by the borehole drilling, the alluvium deposits of the Zagunao river are overlayed by ancient landslide deposits, causing a river-damming event (Figure 8). Due to the strong incising of the river, the landslide dam was eroded and a high-steep free slope surface formed in the toe of the ancient landslide deposits with a height of more than 130 m and an average slope of 40°, resulting in the re-distribution of stress and providing the potential energy of the deformation or even failure. Therefore, the large relief and unique topography facilitated the development of the reactivated landslide and promoted a retrogressive mode for failure.

7.1.2. Triggering Factors and Reactivation Mechanism

- A total of 13 days of heavy precipitation preceding the reactivation

The intense deformation of the reactivated landslide began on 22 June 2020, corresponding to 13 consecutive days of precipitation of 224.5 mm prior to the event. The cumulative rainfall from 10 May to 22 June 2022 reached 546.8 mm, which exceeded 55% of the total annual rainfall. Thus, the long-term rainfall, particularly the last 13 days of the antecedent rainfall period, was the primary triggering factor of this reactivated landslide. The effects of early-stage rainfall include: (1) weakening the mechanical parameters (cohesion and internal friction angle) of the loose ancient landslide deposits; (2) the rise in the river water level reduces the hydraulic gradient of the slope, reduces the amount of groundwater excretion on the slope, and strands a great deal of rainwater on the slope for a long time, thus increasing the self-weight and sliding force of the slope; (3) elevating the groundwater level, leading to a significant reduction in the mechanical parameters at the interface of the foundation cover, causing a sharp drop in the strength of the sliding zone; (4) the dynamic water pressure of long-term rainfall causes the loss of fine-grained soils, enabling a resultant loose structure and poor cohesion, which is more conducive to rainfall infiltration.

- The contribution of anthropogenic activity in changing the strength of the slope

National Road G317 and Wenchuan-Maerkang Highway pass through the slope front in the form of excavation. The highest excavated slope height is about 11 m. The construction of National Road G317 and Wen-Ma Highway reduced the anti-slip section of the slope, forming the steep free face on the slope front, and damaging the strength of the slope. Therefore, anthropogenic activity is the secondary triggering factor of landslide reactivation.

7.2. Integrated Monitor Network on Ancient Landslides in Mountainous Area

The reactivation of the Tangjiawan ancient landslide event was disastrous for road construction and operation in mountainous areas, causing damage to infrastructures and interrupting road operation, consequently leading to severe economic losses. Based on our field investigation, compared with other rainfall- and road excavation-related reactivated landslides in China, such as the Leibo landslide [12,46], Baiyangwan landslide [47], Maobazi landslide [48], and the Dongla landslide [49], the occurrence of such reactivated landslides is particularly related to their complex geological environments [50]. Hence, this event serves as a poignant reminder to diligently consider the spatial distribution and characteristics of active ancient landslides in main road engineering.

The mountainous area in western Sichuan experiences extremely active neotectonics and many strong earthquakes. Numerous ancient landslide deposits are distributed within this area. In order to achieve early detection, real-time monitoring and early warning of reactivated landslides possible along the Wenchuan to Li County section of the Wenchuan-Maerkang Highway. Investigations of these landslides were carried out through employing

optical images, the SBAS-InSAR technique, and field investigations. As depicted in Figure 21, twenty-one ancient landslides are distributed along the highway, which pose a severe threat to the road and surrounding settlements. Efforts are concentrated on the remote measurement of ground surface deformations, in order to define the slope dynamics and landslide activities. Characterization of these ancient landslide deposits remains challenging because of their complex environments and the limitations of monitoring techniques. This paper utilizes an integrated monitor network, appropriately using the outcomes of satellite InSAR, UAV, and in situ monitoring instruments, such as GNSS. These monitoring data from different sources can help identify potentially active ancient landslide deposits preceding road construction and monitor real-time deformation during and after construction. Moreover, for an ancient landslide, which was stable during the construction stage but may be partially revived again due to triggering factors during the operation, the joint analysis could provide a comprehensive overview of the deformation of the landslide, and could evaluate the instability of the landslide in a timely manner, reducing the uncertainties of qualitative analysis.

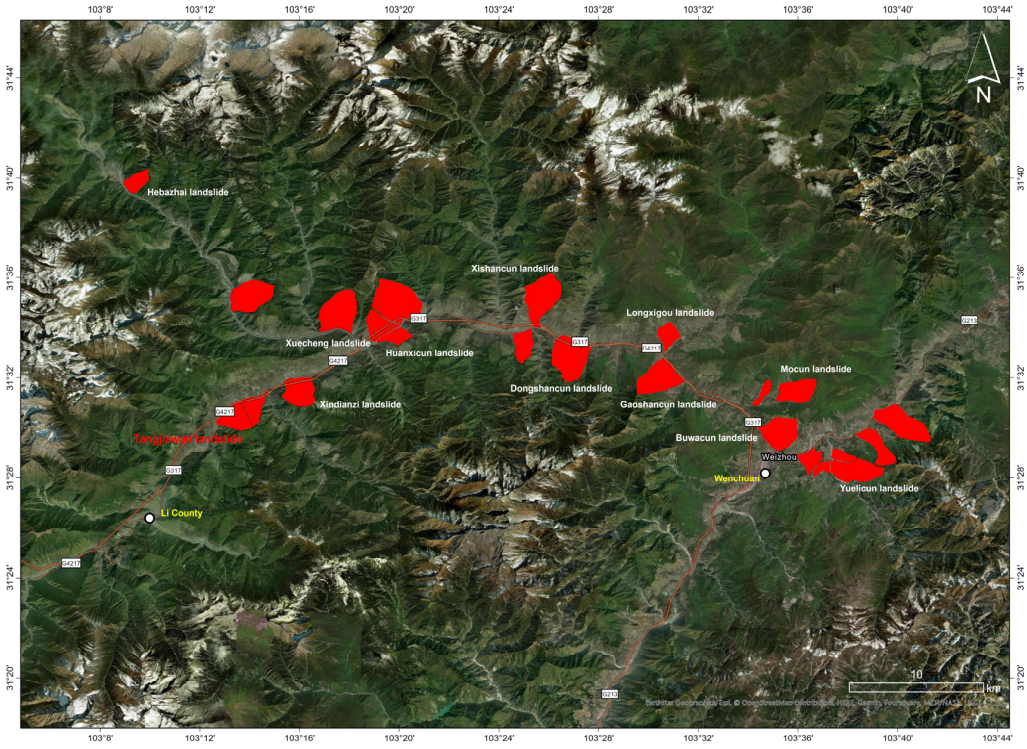

Figure 21. Distribution of ancient landslides on the Wenchuan-Li County section of Wen-Ma Highway from a comprehensive investigation (Red polygons are the ancient landslide areas).

8. Conclusions

This study conducts a detailed investigation on the deformation and mechanisms of a recently reactivated landslide, Tangjiawan landslide in Li County, Sichuan, China. This landslide is located on a steep alpine slope and experienced a large-scale reactivation on 22 June 2020. This event was triggered by a period of prolonged and intense precipitation. By employing an integrated monitoring network, the deformation pre- and post-event, including during the construction of countermeasures, is addressed.

The joint analysis of satellite InSAR, UAV and in situ monitoring data, spanning a time period of four years in total, provided essential insights into the deformation and mechanisms of the reactivated landslide. The landslide activity has been in a state of creep since 2019, with a mean LOS velocity of −18~−5 mm/year. Once the countermeasures were implemented, the deformation rates of the slope were reduced based on the data measured from the GNSS stations, inclinometers and crack meters. The deformation rates were also closely associated with the precipitation.

The reactivation of the landslide is attributed to the loose ancient landslide deposits, fragile geo-structure, and large relief, and it was directly triggered by precipitation, while anthropogenic activity plays a secondary role in its reactivation. Shearing of the sliding mass occurred at a depth of 25.3~40.0 m, exploiting a heavily deformed weak zone composed of breccias with poor permeability.

The distribution and characteristics of ancient landslides along the Wenchuan-Maerkang Highway can be explored using the integrated monitor network, which enables the safe construction and operation of such traffic corridors.

The innovation of this study lies in its comprehensive depiction of the entire spatial-temporal evolution process, from the initiation to the significant deformation, of a reactivated landslide along a major road. This case serves as an excellent reference for analyzing and monitoring similar landslide evolution processes before, during, and after remedial measures are implemented. Furthermore, it demonstrates the integration of remote sensing and continuous surveillance and the establishment of a warning system at potential landslide sites. Consequently, it allows for tracing evolutionary history, generating activity maps, and analyzing development trends with remarkable efficacy in reducing landslide risks.

Author Contributions: Y.D. and K.H. framed the study plan and wrote the paper; Y.D., X.H. and H.M. carried out field surveys; Y.D. conducted the InSAR data treatment; X.H. provided feedback on the manuscript. All authors have read and agreed to the published version of the manuscript.

Funding: This research was funded by the National Natural Science Foundation of China (41907225, 41731285) and the National-funded Postdoctoral Researcher Program of China (GZB20230606).

Data Availability Statement: The original contributions presented in the study are included in the article, further inquiries can be directed to the corresponding author.

Acknowledgments: The authors would like to acknowledge the reviewers for their comments and suggestions, which helped in improving the quality of the manuscript.

Conflicts of Interest: Hongsheng Ma is employed by Sichuan Highway Planning, Survey, Design and Research Institute Ltd. The authors declare no conflict of interest.

References

1. Donnini, M.; Napolitano, E.; Salvati, P.; Ardizzone, F.; Bucci, F.; Fiorucci, F.; Santangelo, M.; Cardinali, M.; Guzzetti, F. Impact of event landslides on road networks: A statistical analysis of two Italian case studies. *Landslides* **2017**, *14*, 1521–1535. [CrossRef]
2. Jaiswal, P.; van Westen, C.J.; Jetten, V. Quantitative assessment of landslide hazard along transportation lines using historical records. *Landslides* **2011**, *8*, 279–291. [CrossRef]
3. Penna, D.; Borga, M.; Aronica, G.T.; Brigandì, G.; Tarolli, P. The influence of grid resolution on the prediction of natural and road-related shallow landslides. *Hydrol. Earth Syst. Sci.* **2014**, *18*, 2127–2139. [CrossRef]
4. Yan, Y.; Cui, Y.; Huang, X.; Zhou, J.; Zhang, W.; Yin, S.; Guo, J.; Hu, S. Combining seismic signal dynamic inversion and numerical modeling improves landslide process reconstruction. *Earth Surf. Dyn.* **2022**, *10*, 1233–1252. [CrossRef]
5. Zhang, Y.; Ayyub, B.M.; Gong, W.; Tang, H. Risk assessment of roadway networks exposed to landslides in mountainous regions—A case study in Fengjie County, China. *Landslides* **2023**, *20*, 1419–1431. [CrossRef]
6. Gu, D.M.; Huang, D.; Yang, W.D.; Zhu, J.L.; Fu, G.Y. Understanding the triggering mechanism and possible kinematic evolution of a reactivated landslide in the Three Gorges Reservoir. *Landslides* **2017**, *14*, 2073–2087. [CrossRef]
7. Lu, N.; Wayllace, A.; Oh, S. Infiltration-induced seasonally reactivated instability of a highway embankment near the Eisenhower Tunnel, Colorado, USA. *Eng. Geol.* **2013**, *162*, 22–32. [CrossRef]
8. Massey, C.I.; Petley, D.N.; McSaveney, M.J. Patterns of movement in reactivated landslides. *Eng. Geol.* **2013**, *159*, 1–19. [CrossRef]
9. Jaafari, A.; Najafi, A.; Rezaeian, J.; Sattarian, A.; Ghajar, I. Planning road networks in landslide-prone areas: A case study from the northern forests of Iran. *Land Use Policy* **2015**, *47*, 198–208. [CrossRef]
10. Sun, D.; Gu, Q.; Wen, H.; Xu, J.; Zhang, Y.; Shi, S.; Xue, M.; Zhou, X. Assessment of landslide susceptibility along mountain highways based on different machine learning algorithms and mapping units by hybrid factors screening and sample optimization. *Gondwana Res.* **2023**, *123*, 89–106. [CrossRef]
11. Tanyaş, H.; Görüm, T.; Kirschbaum, D.; Lombardo, L. Could road constructions be more hazardous than an earthquake in terms of mass movement? *Nat. Hazards* **2022**, *112*, 639–663. [CrossRef]
12. He, K.; Ma, G.; Hu, X.; Luo, G.; Mei, X.; Liu, B.; He, X. Characteristics and mechanisms of coupled road and rainfall-induced landslide in Sichuan China. *Geomat. Nat. Hazards Risk* **2019**, *10*, 2313–2329. [CrossRef]

13. Jiang, N.; Li, H.B.; Hu, Y.X.; Zhang, J.Y.; Dai, W.; Li, C.J.; Zhou, J.W. Dynamic evolution mechanism and subsequent reactivated ancient landslide analyses of the "6.17" Danba sequential disasters. *Bull. Eng. Geol. Environ.* **2022**, *81*, 149. [CrossRef]
14. Lee, C.F.; Huang, W.K.; Chang, Y.L.; Chi, S.Y.; Liao, W.C. Regional landslide susceptibility assessment using multi-stage remote sensing data along the coastal range highway in northeastern Taiwan. *Geomorphology* **2018**, *300*, 113–127. [CrossRef]
15. Barla, G.; Debernardi, D.; Perino, A. Lessons learned from deep-seated landslides activated by tunnel excavation. *Geomech. Tunn.* **2015**, *8*, 394–401. [CrossRef]
16. Carlà, T.; Macciotta, R.; Hendry, M.; Martin, D.; Edwards, T.; Evans, T.; Farina, P.; Intrieri, E.; Casagli, N. Displacement of a landslide retaining wall and application of an enhanced failure forecasting approach. *Landslides* **2018**, *15*, 489–505. [CrossRef]
17. Zhang, Y.; Ren, S.; Liu, X.; Guo, C.; Li, J.; Bi, J.; Ran, L. Reactivation mechanism of old landslide triggered by coupling of fault creep and water infiltration: A case study from the east Tibetan Plateau. *Bull. Eng. Geol. Environ.* **2023**, *82*, 291. [CrossRef]
18. Li, W.; Zhao, B.; Xu, Q.; Yang, F.; Fu, H.; Dai, C.; Wu, X. Deformation characteristics and failure mechanism of a reactivated landslide in Leidashi, Sichuan, China, on August 6, 2019: An emergency investigation report. *Landslides* **2020**, *17*, 1405–1413. [CrossRef]
19. Zhang, Z. Mechanism of the 2019 Yahuokou landslide reactivation in Gansu, China and its causes. *Landslides* **2020**, *17*, 1429–1440. [CrossRef]
20. He, K.; Ma, G.; Hu, X.; Liu, B. Failure mechanism and stability analysis of a reactivated landslide occurrence in Yanyuan City, China. *Landslides* **2021**, *18*, 1097–1114. [CrossRef]
21. Nguyen, L.C.; Tien, P.V.; Do, T.N. Deep-seated rainfall-induced landslides on a new expressway: A case study in Vietnam. *Landslides* **2020**, *17*, 395–407. [CrossRef]
22. Carlà, T.; Tofani, V.; Lombardi, L.; Raspini, F.; Bianchini, S.; Bertolo, D.; Thuegaz, P.; Casagli, N. Combination of GNSS, satellite InSAR, and GBInSAR remote sensing monitoring to improve the understanding of a large landslide in high alpine environment. *Geomorphology* **2019**, *335*, 62–75. [CrossRef]
23. Casagli, N.; Intrieri, E.; Tofani, V.; Gigli, G.; Raspini, F. Landslide detection, monitoring and prediction with remote-sensing techniques. *Nat. Rev. Earth Environ.* **2023**, *4*, 51–64. [CrossRef]
24. Wang, W.; Motagh, M.; Mirzaee, S.; Li, T.; Zhou, C.; Tang, H.; Roessner, S. The 21 July 2020 Shaziba landslide in China: Results from multi-source satellite remote sensing. *Remote Sens. Environ.* **2023**, *295*, 113669. [CrossRef]
25. He, K.; Tanyas, H.; Chang, L.; Hu, X.; Luo, G.; Lombardo, L. Modelling InSAR-derived hillslope velocities with multivariate statistics: A first attempt to generate interpretable predictions. *Remote Sens. Environ.* **2023**, *289*, 113518. [CrossRef]
26. He, K.; Lombardo, L.; Chang, L.; Sadhasivam, N.; Hu, X.; Fang, Z.; Dahal, A.; Fadel, I.; Luo, G.; Tanyas, H. Investigating earthquake legacy effect on hillslope deformation using InSAR-derived time series. *Earth Surf. Process. Landf.* **2024**, *49*, 980–990. [CrossRef]
27. Lacroix, P.; Bièvre, G.; Pathier, E.; Kniess, U.; Jongmans, D. Use of Sentinel-2 images for the detection of precursory motions before landslide failures. *Remote Sens. Environ.* **2018**, *215*, 507–516. [CrossRef]
28. Xie, M.; Zhao, W.; Ju, N.; He, C.; Huang, H.; Cui, Q. Landslide evolution assessment based on InSAR and real-time monitoring of a large reactivated landslide, Wenchuan, China. *Eng. Geol.* **2020**, *277*, 105781. [CrossRef]
29. Bian, S.; Chen, G.; Zeng, R.; Meng, X.; Jin, J.; Lin, L.; Zhang, Y.; Shi, W. Post-failure evolution analysis of an irrigation-induced loess landslide using multiple remote sensing approaches integrated with time-lapse ERT imaging: Lessons from Heifangtai, China. *Landslides* **2022**, *19*, 1179–1197. [CrossRef]
30. Shi, X.; Wang, J.; Jiang, M.; Zhang, S.; Wu, Y.; Zhong, Y. Extreme rainfall-related accelerations in landslides in Danba County, Sichuan Province, as detected by InSAR. *Int. J. Appl. Earth Obs.* **2022**, *115*, 103109. [CrossRef]
31. Cook, M.E.; Brook, M.S.; Hamling, I.J.; Cave, M.; Tunnicliffe, J.F.; Holley, R. Investigating slow-moving shallow soil landslides using Sentinel-1 InSAR data in Gisborne, New Zealand. *Landslides* **2023**, *20*, 427–446. [CrossRef]
32. Dong, J.; Zhang, L.; Li, M.; Yu, Y.; Liao, M.; Gong, J.; Luo, H. Measuring precursory movements of the recent Xinmo landslide in Mao County, China with Sentinel-1 and ALOS-2 PALSAR-2 datasets. *Landslides* **2018**, *15*, 135–144. [CrossRef]
33. Cai, J.; Zhang, L.; Dong, J.; Guo, J.; Wang, Y.; Liao, M. Automatic identification of active landslides over wide areas from time-series InSAR measurements using Faster RCNN. *Int. J. Appl. Earth Obs.* **2023**, *124*, 103516. [CrossRef]
34. van Natijne, A.L.; Bogaard, T.A.; van Leijen, F.J.; Hanssen, R.F.; Lindenbergh, R.C. World-wide InSAR sensitivity index for landslide deformation tracking. *Int. J. Appl. Earth Obs.* **2022**, *111*, 102829. [CrossRef]
35. Xia, Z.; Motagh, M.; Li, T.; Peng, M.; Roessner, S. A methodology to characterize 4D post-failure slope instability dynamics using remote sensing measurements: A case study of the Aniangzhai landslide in Sichuan, Southwest China. *ISPRS J. Photogramm. Remote Sens.* **2023**, *196*, 402–414. [CrossRef]
36. Confuorto, P.; Di Martire, D.; Infante, D.; Novellino, A.; Papa, R.; Calcaterra, D.; Ramondini, M. Monitoring of remedial works performance on landslide-affected areas through ground- and satellite-based techniques. *Catena* **2019**, *178*, 77–89. [CrossRef]
37. Di Maio, C.; Fornaro, G.; Gioia, D.; Reale, D.; Schiattarella, M.; Vassallo, R. In situ and satellite long-term monitoring of the Latronico landslide, Italy: Displacement evolution, damage to buildings, and effectiveness of remedial works. *Eng. Geol.* **2018**, *245*, 218–235. [CrossRef]
38. Nappo, N.; Peduto, D.; Mavrouli, O.; van Westen, C.J.; Gullà, G. Slow-moving landslides interacting with the road network: Analysis of damage using ancillary data, in situ surveys and multi-source monitoring data. *Eng. Geol.* **2019**, *260*, 105244. [CrossRef]

39. Stevens, W.R.; Zehrbach, B.E. Inclinometer Data Analysis for Remediated Landslides. In *Geotechnical Measurements: Lab and Field, Proceedings of Sessions of Geo-Denver 2000, Denver, CO, USA, 5–8 August 2000*; American Society of Civil Engineers: Reston, VA, USA, 2000; Volume 294, pp. 126–137.
40. Lollino, P.; Giordan, D.; Allasia, P.; Fazio, N.L.; Perrotti, M.; Cafaro, F. Assessment of post-failure evolution of a large earthflow through field monitoring and numerical modelling. *Landslides* **2020**, *17*, 2013–2026. [CrossRef]
41. Tang, H.; Li, C.; Hu, X.; Su, A.; Wang, L.; Wu, Y.; Criss, R.; Xiong, C.; Li, Y. Evolution characteristics of the Huangtupo landslide based on in situ tunneling and monitoring. *Landslides* **2015**, *12*, 511–521. [CrossRef]
42. Tildy, P.; Neducza, B.; Nagy, P.; Kanli, A.I.; Hegymegi, C. Time lapse 3D geoelectric measurements for monitoring of in-situ remediation. *J. Appl. Geophys.* **2017**, *136*, 99–113. [CrossRef]
43. Rosen, P.A.; Gurrola, E.; Sacco, G.F.; Zebker, H. The InSAR scientific computing environment. In Proceedings of the EUSAR 2012; 9th European Conference on Synthetic Aperture Radar, Nuremberg, Germany, 23–26 April 2012.
44. Yu, C.; Li, Z.; Penna, N.T.; Crippa, P. Generic Atmospheric Correction Model for Interferometric Synthetic Aperture Radar Observations. *J. Geophys. Res. Solid Earth* **2018**, *123*, 9202–9222. [CrossRef]
45. Hooper, A.; Bekaert, D.; Hussain, E.; Spaans, K. *StaMPS/MTI Manual: Version 4.1b*; School of Earth and Environment, University of Leeds: Leeds, UK, 2018.
46. He, K.; Ma, G.; Hu, X.; Liu, B.; Han, M. The July 2, 2017, Lantian landslide in Leibo, China: Mechanisms and mitigation measures. *Geomech. Eng.* **2022**, *28*, 283–298.
47. Zhang, C.; Yin, Y.; Dai, Z.; Huang, B.; Zhang, Z.; Jiang, X.; Tan, W.; Wang, L. Reactivation mechanism of a large-scale ancient landslide. *Landslides* **2021**, *18*, 397–407. [CrossRef]
48. Zhao, B.; Yuan, L.; Geng, X.; Su, L.; Qian, J.; Wu, H.; Liu, M.; Li, J. Deformation characteristics of a large landslide reactivated by human activity in Wanyuan city, Sichuan Province, China. *Landslides* **2022**, *19*, 1131–1141. [CrossRef]
49. Luo, G.; Hu, X.; Bowman, E.T.; Liang, J. Stability evaluation and prediction of the Dongla reactivated ancient landslide as well as emergency mitigation for the Dongla Bridge. *Landslides* **2017**, *14*, 1403–1418. [CrossRef]
50. Wen, H.; Zhao, S.; Liang, Y.; Wang, S.; Tao, L.; Xie, J. Landslide development and susceptibility along the Yunling–Yanjing segment of the Lancang River using grid and slope units. *Nat. Hazards* **2024**. [CrossRef]

Disclaimer/Publisher's Note: The statements, opinions and data contained in all publications are solely those of the individual author(s) and contributor(s) and not of MDPI and/or the editor(s). MDPI and/or the editor(s) disclaim responsibility for any injury to people or property resulting from any ideas, methods, instructions or products referred to in the content.